Article

Signatures of superconductivity near 80 K in a nickelate under high pressure

https://doi.org/10.1038/s41586-023-06408-7

Received: 13 April 2023

Accepted: 6 July 2023

Published online: 12 July 2023

Check for updates

Hualei Sun[1,7], Mengwu Huo[1,7], Xunwu Hu[1], Jingyuan Li[1], Zengjia Liu[1], Yifeng Han[2], Lingyun Tang[3], Zhongquan Mao[3], Pengtao Yang[4], Bosen Wang[4], Jinguang Cheng[4], Dao-Xin Yao[1], Guang-Ming Zhang[5,6]✉ & Meng Wang[1]✉

Although high-transition-temperature (high-T_c) superconductivity in cuprates has been known for more than three decades, the underlying mechanism remains unknown[1–4]. Cuprates are the only unconventional superconductors that exhibit bulk superconductivity with T_c above the liquid-nitrogen boiling temperature of 77 K. Here we observe that high-pressure resistance and mutual inductive magnetic susceptibility measurements showed signatures of superconductivity in single crystals of $La_3Ni_2O_7$ with maximum T_c of 80 K at pressures between 14.0 GPa and 43.5 GPa. The superconducting phase under high pressure has an orthorhombic structure of *Fmmm* space group with the $3d_{x^2-y^2}$ and $3d_{z^2}$ orbitals of Ni cations strongly mixing with oxygen 2*p* orbitals. Our density functional theory calculations indicate that the superconductivity emerges coincidently with the metallization of the σ-bonding bands under the Fermi level, consisting of the $3d_{z^2}$ orbitals with the apical oxygen ions connecting the Ni–O bilayers. Thus, our discoveries provide not only important clues for the high-T_c superconductivity in this Ruddlesden–Popper double-layered perovskite nickelates but also a previously unknown family of compounds to investigate the high-T_c superconductivity mechanism.

High-transition-temperature (high-T_c) superconductivity in cuprates emerges from hole carriers doped to the Mott insulating state with a half-filled Cu $3d^9$ electronic configuration and $S = 1/2$ spin state[1–4]. As a result of the doping of carriers and metallization of the intra-layer Cu–O electronic σ bonding, the so-called Zhang–Rice singlet forms, leading to the high-T_c superconducting phase[5,6]. At optimal doping, it has been established that superconductivity has a *d*-wave pairing with gap nodes around the Brillouin-zone diagonals[7,8]. Layered structure consisting of corner-connected CuO_6 octahedra and LnO (Ln = lanthanide) layers is a common feature of the high-T_c superconducting materials. Extensive efforts have been made to search for superconductivity in nickel-oxide compounds similar to cuprates[9–11]. Infinite-layer nickelates are one of the extensively investigated families, in which Ni^+ ($3d^9$) shows the same electronic configuration as Cu^{2+} cations. A previous study observed superconductivity with T_c around 9–15 K in $Nd_{0.8}Sr_{0.2}NiO_2$ thin films[12]. Then, superconductivity was observed in other hole-doped $LnNiO_2$ thin films with infinite NiO_2 layers and $Nd_6Ni_5O_{12}$ with quintuple NiO_2 layers[13,14]. The maximum T_c of 31 K has been achieved in $Pr_{0.82}Sr_{0.18}NiO_2$ films at 12.1 GPa, which is below the so-called McMillan limit of 40 K (ref. 15). Superconductivity is observed in the reduced Ruddlesden–Popper phases with the chemical formula $Ln_{n+1}Ni_nO_{2n+2}$; these compounds are obtained from the Ruddlesden–Popper phase $Ln_{n+1}Ni_nO_{3n+1}$ by removing two apical oxygen ions using a topochemical reduction method. A recent study suggests that the unavoidable hydrogen in nickelate films is important for superconductivity[16]. By contrast, no progress has been made on the observation of superconductivity in the Ruddlesden–Popper phase or bulk samples of nickelates[17–19].

Among the Ruddlesden–Popper phase nickelates, the trilayer square planar NiO_2 compounds attracted more attention because the valence state of Ni cations in the reduced Ruddlesden–Popper phase is +1.33, close to +1.2, in which the maximum T_c is expected theoretically[20,21]. In this study, we focus on the bilayer Ruddlesden–Popper bulk single crystals of $La_3Ni_2O_7$ (ref. 22). A simple electron count gives a $Ni^{2.5+}$—that is, $3d^{7.5}$ state for both Ni cations—and experiments indicate that $La_3Ni_2O_7$ is a paramagnetic metal[23]. $Ni^{2.5+}$ is usually given by mixed-valence states of Ni^{2+} ($3d^8$) and Ni^{3+} ($3d^7$), corresponding to the half-filled states of both $3d_{z^2}$ and $3d_{x^2-y^2}$ orbitals and the single-occupied $3d_{z^2}$ orbital, respectively. For the two nearest intra-layer Ni cations in a bilayer Ruddlesden–Popper phase, however, two $3d_{z^2}$ orbitals through apical oxygen usually have a large inter-layer coupling because of the quantum confinement of the NiO_2 bilayer in the structure, and the resulting energy splitting of Ni cations can markedly change the distribution of the averaged valence state of +2.5. First, we synthesized $La_3Ni_2O_7$ single crystals using a high-pressure floating-zone method. The structure of $La_3Ni_2O_7$ crystallizes into an orthorhombic phase (space group *Amam*), with a corner-connected NiO_6 octahedral layer separated by a La–O fluorite-type layer stacking along the *c* axis[22,23] (Fig. 1). Then the structure was investigated at pressures of up to 41.2 GPa, because applying

[1]Center for Neutron Science and Technology, Guangdong Provincial Key Laboratory of Magnetoelectric Physics and Devices, School of Physics, Sun Yat-Sen University, Guangzhou, China. [2]School of Molecular Sciences, Center for Materials of the Universe, Arizona State University, Tempe, AZ, USA. [3]School of Physics and Optoelectronics, South China University of Technology, Guangzhou, China. [4]Beijing National Laboratory for Condensed Matter Physics, Institute of Physics, Chinese Academy of Sciences, Beijing, China. [5]State Key Laboratory of Low-Dimensional Quantum Physics, Department of Physics, Tsinghua University, Beijing, China. [6]Collaborative Innovation Center of Quantum Matter, Beijing, China. [7]These authors contributed equally: Hualei Sun, Mengwu Huo. ✉e-mail: gmzhang@mail.tsinghua.edu.cn; wangmeng5@mail.sysu.edu.cn

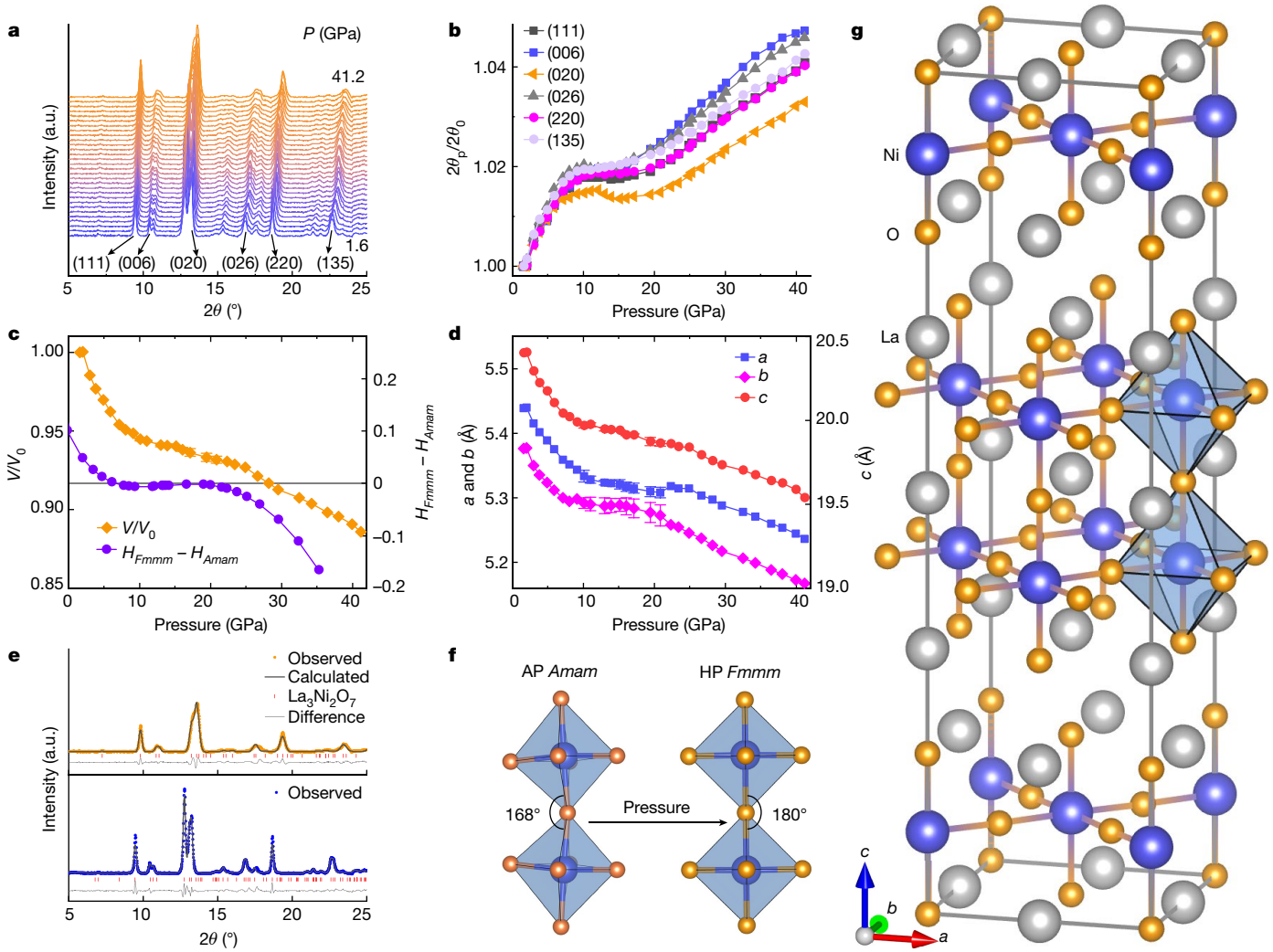

Fig. 1 | Structural characterizations of pressurized $La_3Ni_2O_7$. **a**, Synchrotron XRD patterns of powder samples at various pressures between 1.6 GPa and 41.2 GPa. **b**, Pressure dependence of the peak positions labelled by the Miller indices of the *Amam* space group at ambient pressure. **c**, The orange diamonds represent the change of volume as a function of pressure determined from experiments. The error bars for pressures between 10 GPa and 20 GPa are the volume differences determined from the *Amam* and *Fmmm* space groups, respectively. The violet circles represent the difference in enthalpy of one cell between the space groups *Fmmm* and *Amam* as a function of pressure calculated using the first-principles method. The enthalpy is defined as $H = E(V) + PV$, where $E(V)$ is the energy. The results indicate the ground structure changes to the *Fmmm* space group at high pressures. **d**, Lattice constants *a*, *b* and *c* refined from the XRD patterns. **e**, Refinements of the synchrotron XRD patterns at 29.5 GPa (top) using the space group *Fmmm* and at 1.6 GPa (bottom) using the space group *Amam*. **f**, The Ni–O–Ni angle between two adjacent octahedra shaded in cyan changes from 168° in the ambient-pressure (AP) *Amam* space group to 180° in the high-pressure (HP) *Fmmm* space group. **g**, Crystal structure of $La_3Ni_2O_7$ with the orthorhombic structure. a.u. stands for arbitrary units.

pressure is effective to induce the Jahn–Teller effect through structural modification and electronic band structures. The synchrotron X-ray diffraction (XRD) patterns in the low-pressure phase from 1.6 GPa to 10.0 GPa can be well indexed by the orthorhombic *Amam* space group (Fig. 1a). An anomaly in the positions of the reflection peaks occurs around 10 GPa, suggesting a structural transition (Fig. 1b). Our density functional theory (DFT) calculations indicate that the structure transforms from the *Amam* to the *Fmmm* space group under pressure (Fig. 1c). The XRD patterns in the high-pressure phase above 15.0 GPa can be indexed by the orthorhombic *Fmmm* space group. Evolutions of the lattice parameters and unit cell volume as a function of pressure confirm the structural transition and the DFT calculations (Fig. 1c,d). In particular, the space-group transition corresponds to the change of the bond angle of Ni–O–Ni from 168.0° to 180° along the *c* axis, as depicted in Fig. 1f. X-ray is not sensitive to the position and content of oxygen ions. The structure of the high-pressure phase is determined by a combination of the DFT calculations and the XRD refinements. The structural parameters of $La_3Ni_2O_7$ refined at 1.6 GPa and 29.5 GPa are listed in Extended Data Table 1. The inter-atomic distance between the Ni and apical oxygen is abruptly reduced from 2.297 Å in the *Amam* phase at ambient to 2.122 Å in the *Fmmm* structure at 32.5 GPa (Extended Data Fig. 1).

To explain the electronic structure of $La_3Ni_2O_7$ under pressure, we conducted DFT calculations at 1.6 GPa and 29.5 GPa. The electronic structure can be understood by the crystal-field splitting of the NiO_6 octahedron on the e_g and t_{2g} orbitals of Ni cations[24]. Results of the non-magnetic solution at 1.6 GPa indicate that the electronic states of Ni $3d_{x^2-y^2}$ and $3d_{z^2}$ orbitals are well separated from the other three Ni t_{2g} orbitals in the energy range of −2 eV to 2 eV and that the Ni $3d_{x^2-y^2}$ orbitals with oxygen 2*p* orbitals dominate across the Fermi level (Fig. 2a). The sizes of the hole Fermi surfaces around Γ and the electron Fermi surfaces around Y are comparable[25]. Below and above the Fermi level, there are electronic bonding and anti-bonding bands of the $3d_{z^2}$ electronic states because of the large inter-layer *σ*-bond

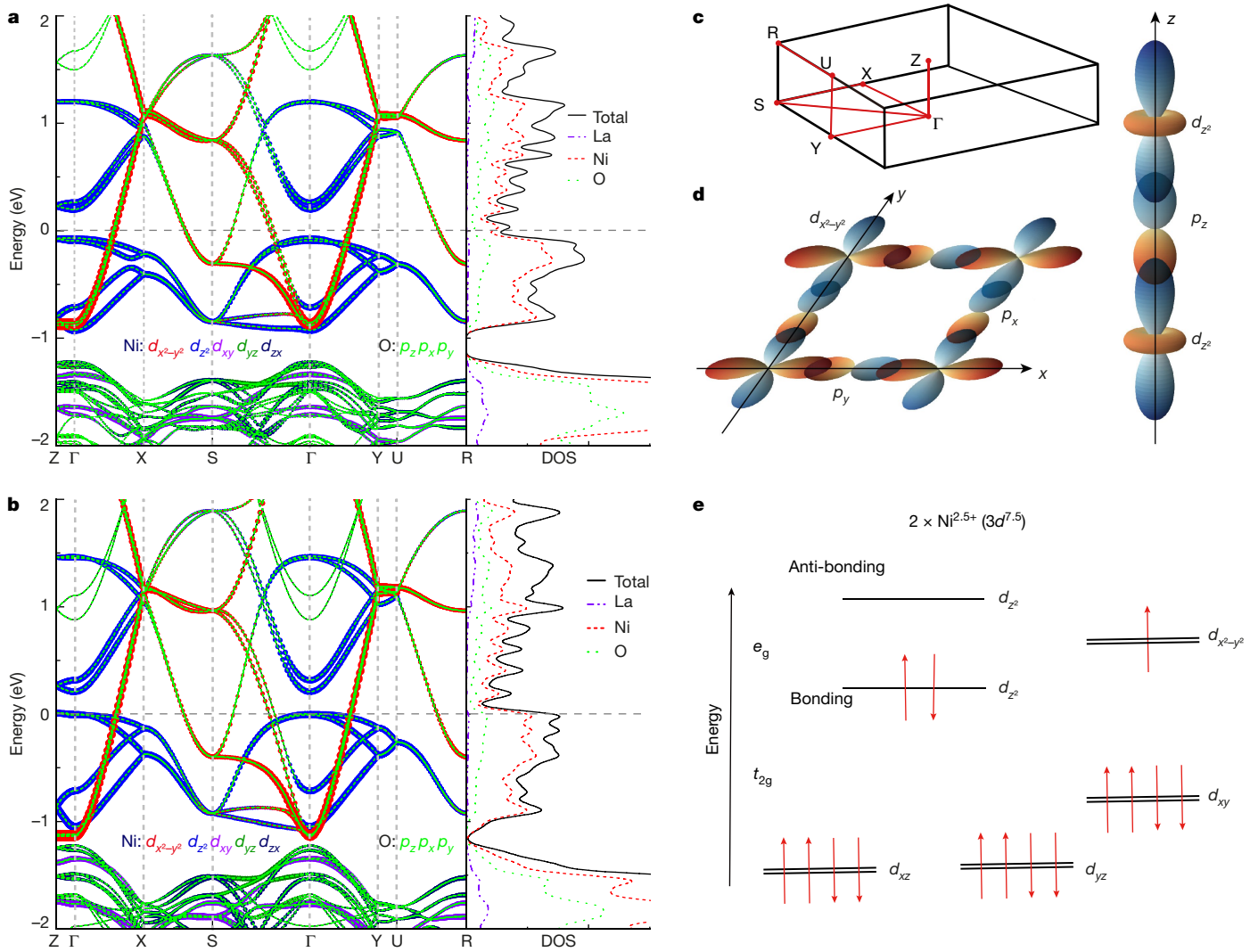

Fig. 2 | DFT calculations for $La_3Ni_2O_7$ at 1.6 GPa and 29.5 GPa. a, Projected electronic band structures of Ni cations and O anions in $La_3Ni_2O_7$ calculated using the structural parameters obtained from the synchrotron XRD at 1.6 GPa and a Coulomb-repulsive $U = 4$ eV. The corresponding density of states (DOS) near the Fermi level are shown on the right. The violet curves represent the contributions from La, red curves from Ni and green curves from O. **b**, Projected electronic band structures and the density of states at 29.5 GPa. **c**, Schematic of the three-dimensional orthorhombic Brillouin zone. The red lines correspond to the paths of the electronic bands in **a** and **b**. **d**, Schematic of the intra-layer σ-bonding states formed by the strong interaction of the Ni $3d_{x^2-y^2}$ and O $2p_{x/y}$ orbitals (left). The inter-layer σ-bonding and anti-bonding states consisting of the Ni $3d_{z^2}$ and O $2p_z$ orbitals (right). **e**, Electronic configuration of two $Ni^{2.5+}$ ($3d^{7.5}$) in the environment of bilayers of NiO_6 octahedra. The d_{z^2} orbitals of two Ni cations in the adjacent layers form the bonding and anti-bonding states.

coupling through an inner apical oxygen (Fig. 2d). There seems to be a band gap because of the quantum confinement of the NiO_2 bilayer in the structure. The splitting makes the $3d_{z^2}$ bonding bands lower in energy and fully occupied, whereas the $3d_{x^2-y^2}$ bands are still degenerate and have a quarter filling (Fig. 2e). Moreover, the bonding $3d_{z^2}$ electronic states form rather flat bands along both the Γ–X and Γ–Y directions, which are the main characteristics of the electronic σ bonds. For the high-pressure phase at 29.5 GPa, however, the $3d_{z^2}$ bonding bands lift upwards crossing the Fermi level as the apical oxygen ions are hole-doped (Fig. 2b) and a small-hole Fermi pocket emerges around the centre of the Brillouin zone (Extended Data Fig. 2), corresponding to the metallization of the lower σ bonds. Furthermore, the same number of electrons is added to the Ni $3d_{x^2-y^2}$ orbitals, increasing their electron occupation as evidenced by the wider proportion of $3d_{x^2-y^2}$ bands below the Fermi level (Fig. 2b). The occupied electrons of Ni $3d_{x^2-y^2}$ orbitals are expected to strongly interact with the $2p$ orbital of oxygen ions, forming the intra-layer Zhang–Rice singlets[5]. The obtained total densities of states reach a maximum at the Fermi energy (Fig. 2b). As high pressure is applied, the electronic interactions between the bilayers of NiO_2 are increased, as evidenced by the enlarged splitting of the $3d_{z^2}$ orbitals at the X and Y points. Therefore, the unique feature of the pressurized electronic structure makes the filling of electrons for the two $Ni^{2.5+}$ cations resemble that of Cu^{2+} ($3d^9$) in hole-doped bilayer cuprates[26]. The metallization of the inter-layer σ-bonding bands shows the emergence of conventional high-T_c superconductivity in MgB_2, $Li_3B_4C_2$, H_3S and other hydrogen-enriched compounds[27–29], enabling us to explore the possible superconductivity in the high-pressure phase of $La_3Ni_2O_7$.

Figure 3a shows the temperature dependence of the resistance for $La_3Ni_2O_7$ single crystals in the pressure range of 0–18.5 GPa. At ambient pressure, $La_3Ni_2O_7$ is metallic and behaves like a Fermi liquid. The anomalies in resistance that suggest the existence of charge-density wave observed previously in polished 80-μm thick samples cannot be clearly observed in the unpolished sample[23] (Fig. 3a). The single crystals used for high-pressure measurements were taken from the sample measured at ambient pressure. A pressure of 1.0 GPa can change the

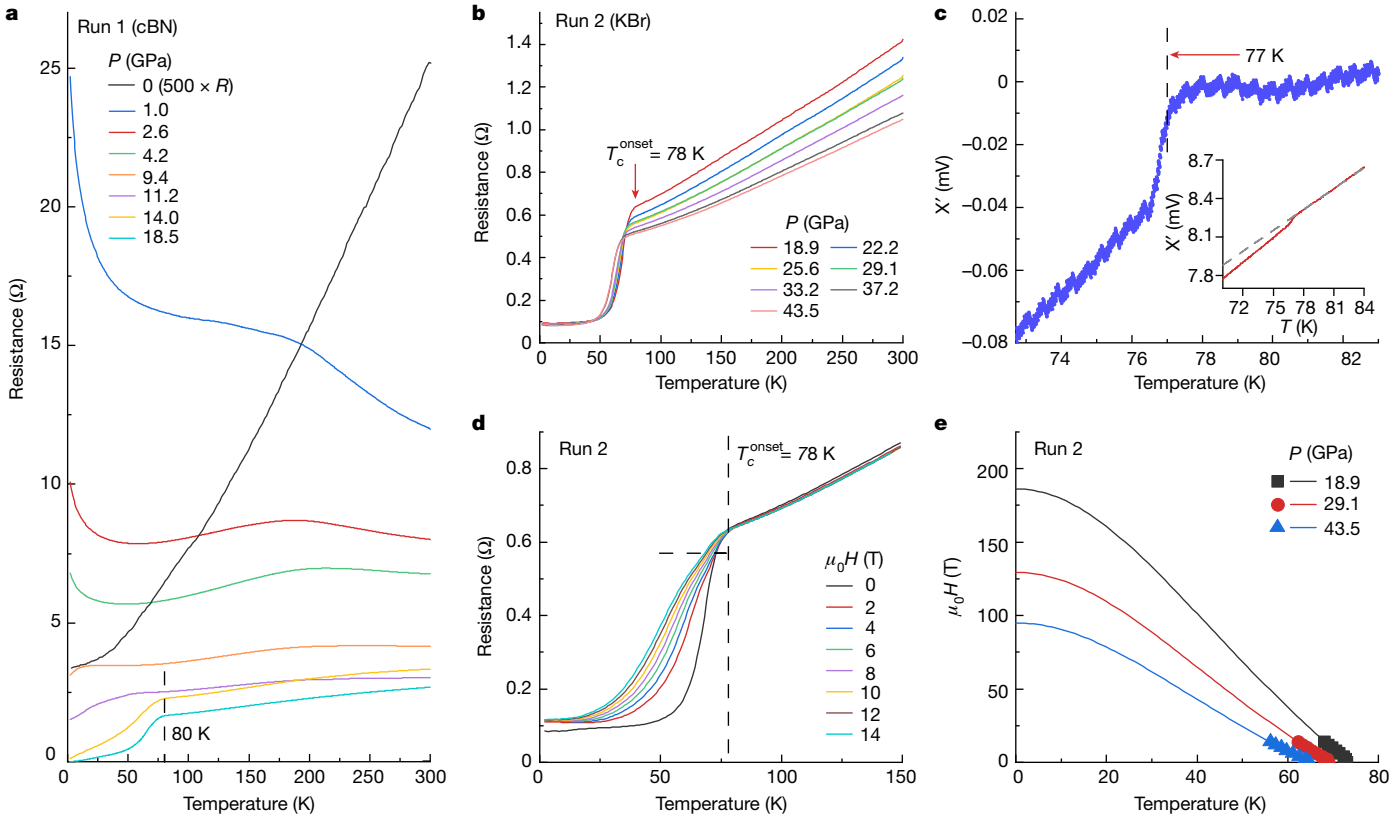

Fig. 3 | Superconducting transitions in $La_3Ni_2O_7$ single crystals under pressure. a, Resistance of $La_3Ni_2O_7$ versus temperature at different pressures from 1.0 GPa to 18.5 GPa with the gasket of cubic boron nitride (cBN) and epoxy mixture. The resistance at ambient pressure was measured independently in an unpolished sample. **b**, High-pressure resistance measurements using KBr as the pressure-transmitting medium. The arrow shows the onset superconducting transition temperature (T_c). The onset T_c at 18.9 GPa is 78 K. **c**, The background-subtracted real part of the a.c. susceptibility showing a prominent diamagnetic response at 25.2 GPa with a current frequency of 393 Hz and a magnitude of 50 mA. The red solid line in the inset shows the raw data and the grey dashed line is a fitted background following the trend above the transition at 77 K. The vertical dashed line marks the T_c. **d**, Resistance curves below 150 K at different magnetic fields from 0 T to 14 T at 18.9 GPa. The vertical dashed lines show the onset T_c. The horizontal line in **d** indicates 90% of the resistance at the onset T_c, $0.9 \times R(T_c^{onset})$. The currents used are 10 μA (**a**), 300 μA (**b**) and 300 μA (**d**). **e**, The Ginzburg–Landau fittings of the upper critical fields, μ_0H_{c2} at pressures of 18.9 GPa, 29.1 GPa and 43.5 GPa using $0.9 \times R(T_c^{onset})$ for run 2. The maximum μ_0H_{c2} for 18.9 GPa is 186 T. The magnetic fields are applied along the *c* direction.

ground state from metallic to weakly insulating, consistent with previous reports[30,31]. The increase of resistance under a small pressure could be ascribed to the distortion of the NiO_6 octahedra[32]. With further increase in pressure, $La_3Ni_2O_7$ undergoes a weakly insulating to metallic transition at about 10 GPa, and a clear drop in resistance at about 78.2 K is observed at pressures above 14.0 GPa, indicating a superconducting-like phase transition. The temperatures of the drop are weakly pressure dependent, reaching 80 K at 18.5 GPa. Above T_c, the resistance increases linearly up to 300 K, which is a typical property of a strange metal state characterizing the normal state of the optimally doped cuprate superconductors[33]. As pressure gradient and internal strain effect could affect the electrical transport properties under pressure, as observed in $K_{0.8}Fe_{1.7}Se_2$ (ref. 34) and $BaFe_2S_3$ (ref. 35), we used a soft material KBr as the pressure-transmitting medium, and the resistance is measured at higher pressures (Fig. 3b). The sharp drops in resistance and the flat resistance that approaches zero below T_c suggest a superconducting transition. The behaviours of resistance are repeatable, as shown in Extended Data Fig. 3.

To show the diamagnetic property of our samples under high pressure, we measured the inductive voltage, which can be regarded as a.c. magnetic susceptibility[36], for the $La_3Ni_2O_7$ single crystal under pressures up to 28.7 GPa using a diamond anvil cell and a mutual induction method[37]. There is a diamagnetic response below 77 K at 25.2 GPa from the real part of the a.c. magnetic susceptibility $\chi'(T)$, as shown in Fig. 3c. The measured electronic and magnetic properties demonstrate that the transition near 80 K corresponds to the emergence of superconductivity. Magnetic susceptibility below 14.3 GPa was also measured by adopting a palm-type cubic anvil cell. No detectable diamagnetic response corresponds to the weak and broad drops in resistance at 9.4 GPa and 11.2 GPa in Fig. 3a. Figure 3d shows the evolution of the resistance at 18.9 GPa under various magnetic fields up to 14 T. The field-suppressed superconductivity is more pronounced at lower temperatures. This is comparable to that of the cuprate superconductors, in which the onset T_c is kept unchanged[38]. The upper critical field $\mu_0H_{c2}(0)$ of $La_3Ni_2O_7$ has been determined using the criterion of $0.9 \times R(T_c^{onset})$, where $R(T_c^{onset})$ is the resistance at the onset T_c. The Ginzburg–Landau formula is adopted for fitting μ_0H_{c2} at various pressures, yielding the highest $\mu_0H_{c2} = 186$ T for 18.9 GPa (Fig. 3e). An estimation of the in-plane superconducting coherence length is 4.83 nm for 18.9 GPa at zero temperature.

The electrical and magnetic measurements under high pressure were repeated on several single-crystal samples (Extended Data Figs. 3–5). The corresponding T_c values are summarized in the temperature–pressure phase diagram in Fig. 4. The transition from a weak insulating phase to a superconducting phase against pressure is similar to the hole-doping dependence of superconductivity in the infinite-layer nickelate films[16,39–41]. But the superconductivity with a high transition temperature above the liquid-nitrogen boiling point of 80 K emerges in the orthorhombic *Fmmm* phase, and the T_c values are not markedly changed in the superconducting region. The normal state of the superconductivity shows a strange metal behaviour that is characterized by a linear

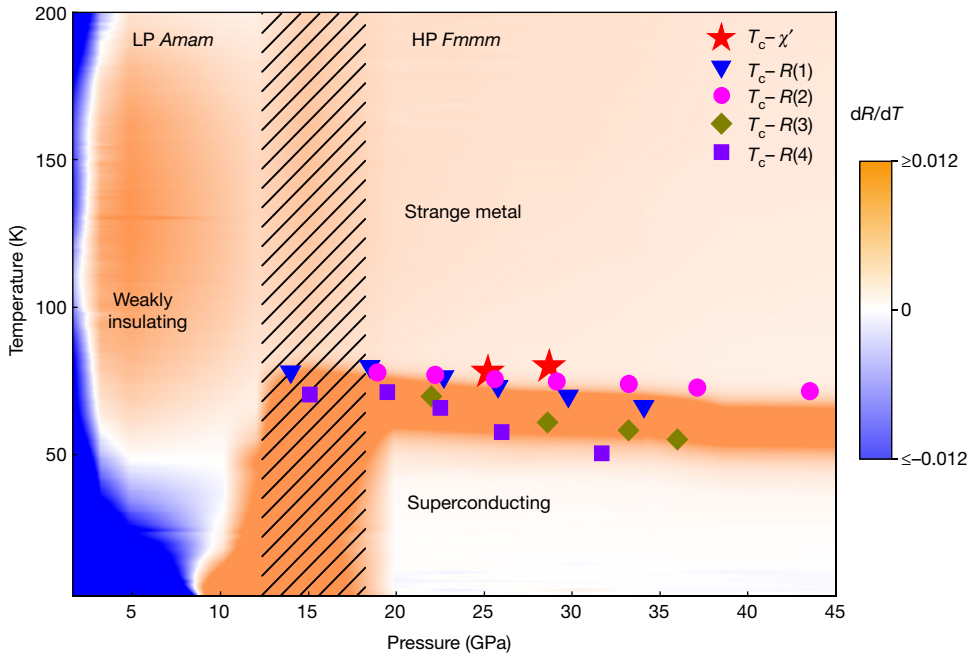

Fig. 4 | Phase diagram of the high-temperature superconductivity in $La_3Ni_2O_7$ single crystals. The superconducting transition temperature, T_c, as a function of pressure obtained from our resistance and inductive magnetic susceptibility measurements. The colours of the background refer to the derivative of the resistance with respect to temperature in Fig. 3a,b. The blue colour with negative values of dR/dT indicates the decrease in resistivity with increasing temperature. The homogeneous colour against temperature in the strange metal area indicates the linear temperature-dependent resistance. The shaded stripe indicates a structural transition from the low-pressure (LP) orthorhombic *Amam* phase to the high-pressure (HP) *Fmmm* phase.

temperature-dependent resistance up to 300 K. This may indicate that the high-pressure metallic phase is close to a quantum critical regime.

We note that some samples are insulating at low pressures and cannot be tuned to metallic state up to 20 GPa. These should be related to the presence of slightly deficient oxygen ions in $La_3Ni_2O_{7-\delta}$. Previous experiments have shown that when the oxygen-deficient variant $0.08 \le \delta \le 0.63$, a phase transition of the structure occurs from orthorhombic to tetragonal symmetry and the electrical transport properties change from metallic to weakly insulating at ambient pressure[42,43]. With regard to the metallic behaviour of our superconducting samples, the deficient oxygen variant δ should be less than 0.08.

In summary, we have shown that the electronic occupancy of $Ni^{2.5+}$ ($3d^{7.5}$) in the Ruddlesden–Popper double-layered perovskite nickelate $La_3Ni_2O_7$ can mimic the Cu^{2+} of hole-doped bilayer high-T_c cuprates because of the presence of strong inter-layer coupling of $3d_{z^2}$ orbitals using the apical oxygen anions. This inter-layer coupling results in the formation of the inter-layer σ-bonding and anti-bonding bands lying below and above the Fermi level. Applying a high pressure can realize the metallization of the σ-bonding bands below the Fermi level through hole doping in the $3d_{z^2}$ orbitals and electron doping in the $3d_{x^2-y^2}$ orbitals. These are the most important indicators of the high-T_c superconductivity with $T_c \approx 80$ K observed in $La_3Ni_2O_7$ single crystals above 14 GPa. Although both $3d_{x^2-y^2}$ and $3d_{z^2}$ orbitals are involved, these features are distinctly different from the infinite-layer superconducting nickelates, in which the electronic states of oxygen 2p orbitals are far below the Fermi level and have a much reduced 3d–2p mixing because of the larger separation of their site energies. In our experiments, T_c is comparable with that of the high-T_c cuprate superconductors[1,4] and higher than the record T_c of the iron-based superconductors[44]. This is one of the first experimental reports on the signatures of superconductivity in both bulk nickelates and the Ruddlesden–Popper phase of nickelates. Our results indicate that the nickel-oxide system enables the study of high-T_c superconductors and helps in understanding its unconventional high-T_c superconductivity mechanism.

Online content

Any methods, additional references, Nature Portfolio reporting summaries, source data, extended data, supplementary information, acknowledgements, peer review information; details of author contributions and competing interests; and statements of data and code availability are available at https://doi.org/10.1038/s41586-023-06408-7.

1. Bednorz, J. G. & Müller, K. A. Possible highT_c superconductivity in the Ba–La–Cu–O system. *Z. Phys. B Condens. Matter* **64**, 189–193 (1986).
2. Anderson, P. W. The resonating valence bond state in La_2CuO_4 and superconductivity. *Science* **235**, 1196–1198 (1987).
3. Lee, P. A., Nagaosa, N. & Wen, X.-G. Doping a Mott insulator: physics of high-temperature superconductivity. *Rev. Mod. Phys.* **78**, 17–85 (2006).
4. Keimer, B., Kivelson, S. A., Norman, M. R., Uchida, S. & Zaanen, J. From quantum matter to high-temperature superconductivity in copper oxides. *Nature* **518**, 179–186 (2015).
5. Zhang, F. C. & Rice, T. M. Effective Hamiltonian for the superconducting Cu oxides. *Phys. Rev. B* **37**, 3759–3761 (1988).
6. Gao, M., Lu, Z.-Y. & Xiang, T. Finding high-temperature superconductors by metallizing the σ-bonding electrons. *Physics* **44**, 421–426 (2015).
7. Shen, Z.-X. et al. Anomalously large gap anisotropy in the *a*-*b* plane of $Bi_2Sr_2CaCu_2O_{8+\delta}$. *Phys. Rev. Lett.* **70**, 1553–1556 (1993).
8. Wollman, D. A., Van Harlingen, D. J., Lee, W. C., Ginsberg, D. M. & Leggett, A. J. Experimental determination of the superconducting pairing state in YBCO from the phase coherence of YBCO-Pb dc SQUIDs. *Phys. Rev. Lett.* **71**, 2134–2137 (1993).
9. Hayward, M. A., Green, M. A., Rosseinsky, M. J. & Sloan, J. Sodium hydride as a powerful reducing agent for topotactic oxide deintercalation: synthesis and characterization of the nickel(I) oxide $LaNiO_2$. *J. Am. Chem. Soc.* **121**, 8843–8854 (1999).
10. Boris, A. V. et al. Dimensionality control of electronic phase transitions in nickel-oxide superlattices. *Science* **332**, 937–940 (2011).
11. Disa, A. S. et al. Orbital engineering in symmetry-breaking polar heterostructures. *Phys. Rev. Lett.* **114**, 026801 (2015).
12. Li, D. et al. Superconductivity in an infinite-layer nickelate. *Nature* **572**, 624–627 (2019).
13. Osada, M., Wang, B. Y., Lee, K., Li, D. & Hwang, H. Y. Phase diagram of infinite layer praseodymium nickelate $Pr_{1-x}Sr_xNiO_2$ thin films. *Phys. Rev. Mater.* **4**, 121801 (2020).
14. Pan, G. A. et al. Superconductivity in a quintuple-layer square-planar nickelate. *Nat. Mater.* **21**, 160–164 (2022).
15. Wang, N. N. et al. Pressure-induced monotonic enhancement of T_c to over 30 K in superconducting $Pr_{0.82}Sr_{0.18}NiO_2$ thin films. *Nat. Commun.* **13**, 4367 (2022).
16. Ding, X. et al. Critical role of hydrogen for superconductivity in nickelates. *Nature* **615**, 50–55 (2023).

17. Li, Q. et al. Absence of superconductivity in bulk $Nd_{1-x}Sr_xNiO_2$. *Commun. Mater.* **1**, 16 (2020).
18. Wang, B.-X. et al. Synthesis and characterization of bulk $Nd_{1-x}Sr_xNiO_2$ and $Nd_{1-x}Sr_xNiO_3$. *Phys. Rev. Mater.* **4**, 084409 (2020).
19. Huo, M. et al. Synthesis and properties of $La_{1-x}Sr_xNiO_3$ and $La_{1-x}Sr_xNiO_2$. *Chin. Phys. B* **31**, 107401 (2022).
20. Nica, E. M. et al. Theoretical investigation of superconductivity in trilayer square-planar nickelates. *Phys. Rev. B* **102**, 020504 (2020).
21. Lechermann, F. Multiorbital processes rule the $Nd_{1-x}Sr_xNiO_2$ normal state. *Phys. Rev. X* **10**, 041002 (2020).
22. Voronin, V. I. et al. Neutron diffraction, synchrotron radiation and EXAFS spectroscopy study of crystal structure peculiarities of the lanthanum nickelates $La_{n+1}Ni_nO_y$ (n=1,2,3). *Nucl. Instrum. Methods Phys. Res. A* **470**, 202–209 (2001).
23. Liu, Z. et al. Evidence for charge and spin density waves in single crystals of $La_3Ni_2O_7$ and $La_3Ni_2O_6$. *Sci. Chin. Phys. Mech. Astron.* **66**, 217411 (2023).
24. Pardo, V. & Pickett, W. E. Metal-insulator transition in layered nickelates $La_3Ni_2O_{7-\delta}$ (δ=0.0, 0.5, 1). *Phys. Rev. B* **83**, 245128 (2011).
25. Adhikary, P., Bandyopadhyay, S., Das, T., Dasgupta, I. & Saha-Dasgupta, T. Orbital-selective superconductivity in a two-band model of infinite-layer nickelates. *Phys. Rev. B* **102**, 100501 (2020).
26. Sakakibara, H. et al. Orbital mixture effect on the Fermi-surface–T_c correlation in the cuprate superconductors: bilayer vs. single layer. *Phys. Rev. B* **89**, 224505 (2014).
27. Choi, H. J., Roundy, D., Sun, H., Cohen, M. L. & Louie, S. G. The origin of the anomalous superconducting properties of MgB_2. *Nature* **418**, 758–760 (2002).
28. Gao, M., Lu, Z.-Y. & Xiang, T. Prediction of phonon-mediated high-temperature superconductivity in $Li_3B_4C_2$. *Phys. Rev. B* **91**, 045132 (2015).
29. Drozdov, A. P. et al. Superconductivity at 250 K in lanthanum hydride under high pressures. *Nature* **569**, 528–531 (2019).
30. Wu, G., Neumeier, J. J. & Hundley, M. F. Magnetic susceptibility, heat capacity, and pressure dependence of the electrical resistivity of $La_3Ni_2O_7$ and $La_4Ni_3O_{10}$. *Phys. Rev. B* **63**, 245120 (2001).
31. Hosoya, T. et al. Pressure studies on the electrical properties in $R_{2-x}Sr_xNi_{1-y}Cu_yO_{4+\delta}$ (R=La, Nd) and $La_3Ni_2O_{7+\delta}$. *J. Phys. Conf. Ser.* **121**, 052013 (2008).
32. Mochizuki, Y., Akamatsu, H., Kumagai, Y. & Oba, F. Strain-engineered Peierls instability in layered perovskite $La_3Ni_2O_7$ from first principles. *Phys. Rev. Mater.* **2**, 125001 (2018).
33. Yuan, J. et al. Scaling of the strange-metal scattering in unconventional superconductors. *Nature* **602**, 431–436 (2022).
34. Sun, L. et al. Re-emerging superconductivity at 48 kelvin in iron chalcogenides. *Nature* **483**, 67–69 (2012).
35. Takahashi, H. et al. Pressure-induced superconductivity in the iron-based ladder material $BaFe_2S_3$. *Nat. Mater.* **14**, 1008–1012 (2015).
36. Deemyad, S. & Schilling, J. S. Superconducting phase diagram of Li metal in nearly hydrostatic pressures up to 67 GPa. *Phys. Rev. Lett.* **91**, 167001 (2003).
37. Chen, X. J. et al. Enhancement of superconductivity by pressure-driven competition in electronic order. *Nature* **466**, 950–953 (2010).
38. Chu, C. W. et al. Superconductivity above 150 K in $HgBa_2Ca_2Cu_3O_{8+\delta}$ at high pressures. *Nature* **365**, 323–325 (1993).
39. Gu, Q. & Wen, H.-H. Superconductivity in nickel-based 112 systems. *Innovation* **3**, 100202 (2022).
40. Zeng, S. et al. Superconductivity in infinite-layer nickelate $La_{1-x}Ca_xNiO_2$ thin films. *Sci. Adv.* **8**, eabl9927 (2022).
41. Hsu, Y.-T. et al. Insulator-to-metal crossover near the edge of the superconducting dome in $Nd_{1-x}Sr_xNiO_2$. *Phys. Rev. Res.* **3**, L042015 (2021).
42. Zhang, Z., Greenblatt, M. & Goodenough, J. B. Synthesis, structure, and properties of the layered perovskite $La_3Ni_2O_{7-\delta}$. *J. Solid State Chem. Solids.* **108**, 402–409 (1994).
43. Taniguchi, S. et al. Transport, magnetic and thermal properties of $La_3Ni_2O_{7-\delta}$. *J. Phys. Soc. Jpn.* **64**, 1644–1650 (1995).
44. Zhi-An, R. et al. Superconductivity at 55 K in iron-based F-doped layered quaternary compound $Sm[O_{1-x}F_x]$ FeAs. *Chin. Phys. Lett.* **25**, 2215–2216 (2008).

Methods

Material synthesis

$La_3Ni_2O_7$ single crystals were grown using a vertical optical-image floating-zone furnace at an oxygen pressure of 15 bar and a 5-kW Xenon arc lamp (100-bar Model HKZ, SciDre)[23].

High-pressure synchrotron X-ray experiments

High-pressure synchrotron radiation XRD data were collected at 300 K with a wavelength λ = 0.6199 Å at the Beijing Synchrotron Radiation Facility. An asymmetric diamond anvil cell (DAC) with a pair of 300-μm-diameter culets was used. The steel gasket was pre-indented and a diameter of 110 μm was laser-drilled at the centre to serve as a sample chamber. The samples were ground into powder and a ruby sphere was loaded in the middle of the sample chamber and silicone oil was used as a pressure-transmitting medium. The pressure was calibrated by measuring the shift of its fluorescence wavelength. The data were initially integrated using Dioptas (with a CeO_2 calibration)[45] and the subsequent Rietveld refinements were processed using TOPAS-Academic[46].

High-pressure electrical property measurements

The electrical resistance measurements of $La_3Ni_2O_7$ single crystals were performed using the standard four-probe method. High pressure was generated with screw-pressure-type DAC made of nonmagnetic Be–Cu alloy. Diamond anvils with a 400-μm culet were used, and the corresponding sample chamber with a diameter of 150 μm was made in an insulating gasket achieved by cubic boron nitride and epoxy mixture. A single crystal with a dimension of 80 × 60 × 10 μm^3 was loaded without pressure-transmitting medium in run 1. Fine KBr powders as the pressure-transmitting medium and a single crystal of the same size were adopted in run 2. Pressure was calibrated using the ruby fluorescence shift at room temperature for all experiments. Electrical measurements were taken on a physical property measurement system (PPMS, Quantum Design) providing synergetic extreme environments with temperatures from 2 K to 300 K and magnetic fields up to 14 T.

The observed transitions and residual resistance depend on the pressure-transmitting medium because of the homogeneity of pressure. The resistance of different single-crystal samples of $La_3Ni_2O_7$ in run 1, run 3 and run 4 under pressure is measured without a pressure-transmitting medium. The transitions are broad down to 2 K. The transitions in resistance of run 2 with KBr become sharper. Moreover, a flat stage in resistance below the transition temperature is observed, indicating a superconducting transition. The flat stage is not expected for the emergent orders such as charge-density wave and spin-density wave. We note that there is only a small drop in resistance for the superconducting transition in $BaFe_2S_3$ under pressure measured using NaCl as the pressure-transmitting medium. Zero resistance is achieved by replacing a liquid transmitting medium such as glycerine[35]. However, high-pressure electrical measurement using the liquid transmitting medium is technologically challenging. The nonzero resistance of $La_3Ni_2O_7$ under pressure below the transition may also be related to the inhomogeneity of the stoichiometry—in particular, the deviation of the oxygen content.

Magnetic susceptibility measurements

The a.c. magnetic susceptibility up to 14.3 GPa using a palm-type cubic anvil cell was measured at the Synergetic Extreme Condition User Facility. For these measurements, no discernible anomaly could be detected (Extended Data Fig. 6). We then measured the a.c. magnetic susceptibility up to 28.7 GPa using a magnetic inductive technique[34,36] in the School of Physics and Optoelectronics, South China University of Technology. The 600-μm diamond culets and the corresponding sample chamber with a diameter of 180 μm were made in a nonmagnetic Be–Cu gasket. The sample chamber was filled with fine $La_3Ni_2O_7$ powder without any other pressure-transmitting medium. Pressure values were estimated from the calibration curve determined by the ruby fluorescence wavelength at 300 K. This magnetic inductive technique consists of three parts—exciting coil, pickup coil and compensating coil. The a.c. in the exciting coil of 100 turns with a diameter of 8.5 mm is fed from a Stanford Research SR830 digital lock-in amplifier. The corresponding excitation field is about 9 oersted. Inside the excitation coil, a pickup coil of 100 turns with a diameter of 2.0 mm is wounded around the sample, and a compensating coil is oppositely connected next to it. The alternating magnetic field generates electromotive forces in the pickup coil, which is detected by Keithley 2182A. The detected signal is a superposition of the susceptibility of the metallic parts of the DAC and the susceptibility of the sample.

DFT calculations

The first-principles calculations were performed using the DFT as indicated in the Vienna ab initio simulation package[47]. The projector augmented-wave method[48] with a 600-eV plane-wave kinetic cut-off energy was used. The generalized gradient approximation of Perdew–Burke–Ernzerhof[49] form was used for exchange-correlation functional. A 19 × 19 × 5 k-points mesh was used for the self-consistent and Fermi surface calculations. The lattice parameters were fixed to the experimentally refined lattice constants obtained from XRD. The atomic positions were fully optimized until forces on each atom were less than 0.001 eV $Å^{-1}$, and the energy convergence criterion was set at 10^{-6} eV for the electronic self-consistent loop.

For the DFT + U treatment of Ni 3d electrons in $La_3Ni_2O_7$, the U parameter was estimated to be 5.9 eV using the linear-response method. We tested the U values with 4 eV, 5 eV and 6 eV, which gave similar results. Finally, an effective Hubbard U for the 3d electrons of Ni cations was chosen as 4 eV in this study[50]. The energies as a function of volume ($E(V)$) were calculated from the first-principles calculations. The volume of the unit cell was fixed using the experimental lattice parameters, and the atomic positions were fully optimized. The Murnaghan equation was used to fit the E–V data. The pressure dependence of the enthalpy can be written as $H = E(V) + PV$. The ground-state phase was determined from the enthalpy.

Data availability

Source data are provided with this paper.

45. Prescher, C. & Prakapenka, V. B. DIOPTAS: a program for reduction of two-dimensional X-ray diffraction data and data exploration. *High Press. Res.* **35**, 223–230 (2015).
46. Coelho, A. A. TOPAS and TOPAS-Academic: an optimization program integrating computer algebra and crystallographic objects written in C++. *J. Appl. Crystallogr.* **51**, 210–218 (2018).
47. Kresse, G. & Furthmüller, J. Efficient iterative schemes for ab initio total-energy calculations using a plane-wave basis set. *Phys. Rev. B* **54**, 11169–11186 (1996).
48. Blochl, P. E. Projector augmented-wave method. *Phys. Rev. B* **50**, 17953–17979 (1994).
49. Perdew, J. P., Burke, K. & Ernzerhof, M. Generalized gradient approximation made simple. *Phys. Rev. Lett.* **77**, 3865–3868 (1996).
50. Dudarev, S. L., Botton, G. A., Savrasov, S. Y., Humphreys, C. J. & Sutton, A. P. Electron-energy-loss spectra and the structural stability of nickel oxide: an LSDA+U study. *Phys. Rev. B* **57**, 1505–1509 (1998).

Acknowledgements M.W. acknowledges the support of the National Natural Science Foundation of China (grant no. 12174454), the Guangdong Basic and Applied Basic Research Funds (grant no. 2021B1515120015) and the Guangdong Provincial Key Laboratory of Magnetoelectric Physics and Devices (grant no. 2022B1212010008). H.S. acknowledges the support of the Guangzhou Basic and Applied Basic Research Funds (grant no. 202201011123). D.-X.Y. is supported by NKRDPC-2022YFA1402802, NKRDPC-2018YFA0306001, NSFC-92165204, NSFC-11974432 and the Shenzhen International Quantum Academy. P.Y., B.W. and J.C. are supported by the National Natural Science Foundation of China (grant nos 12025408 and 11921004), the Beijing Natural Science Foundation (grant no. Z190008), the National Key R&D Program of China (grant no. 2021YFA1400200) and the Strategic Priority Research Program of CAS (grant no. XDB33000000). A portion of this work was carried out at the Synergetic Extreme Condition User Facility. High-pressure synchrotron X-ray measurements were performed at the 4W2 High-Pressure Station, Beijing Synchrotron Radiation Facility,

which is supported by the Chinese Academy of Sciences (grant nos. KJCX2-SW-N20 and KJCX2-SW-N03).

Author contributions M.W. designed the project; Z.L. and M.H. grew the single crystals; H.S., M.H. and J.L. performed the resistance measurements at varying pressures; H.S. performed the synchrotron XRD measurements; H.S. and J.L. conducted the high-pressure susceptibility measurements with the support of L.T. and Z.M.; magnetic susceptibility for pressures below 14 GPa (data not shown) was measured with the support of P.Y., B.W. and J.C.; H.S., Y.H. and M.H. conducted the structural analysis; D.-X.Y. and X.H. performed the DFT calculations. G.-M.Z. proposed a relevant physical picture to understand both the numerical and experimental results. M.W. and G.-M.Z. wrote the paper with inputs from all co-authors.

Competing interests The authors declare no competing interests.

Additional information

Supplementary information The online version contains supplementary material available at https://doi.org/10.1038/s41586-023-06408-7.

Correspondence and requests for materials should be addressed to Guang-Ming Zhang or Meng Wang.

Peer review information *Nature* thanks the anonymous reviewers for their contribution to the peer review of this work. Peer reviewer reports are available.

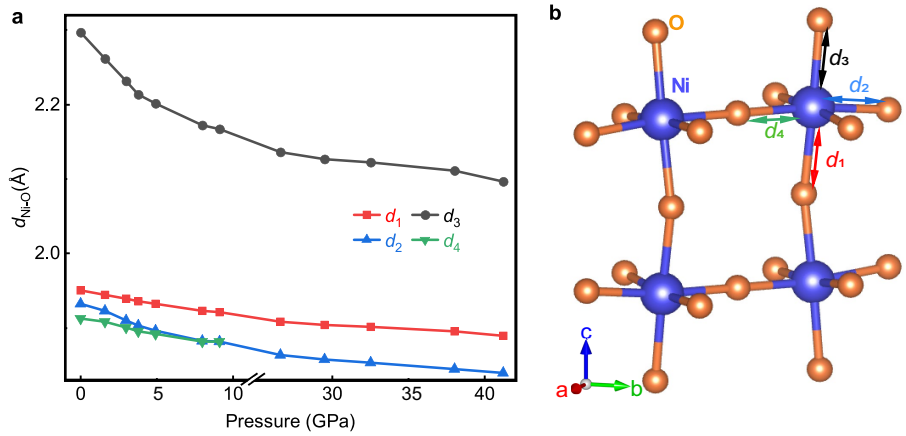

Extended Data Fig. 1 | Ni-O distances in the NiO_6 octahedra of $La_3Ni_2O_7$ under pressure. a, Ni-O distances against pressure. The lattice constants are refined from synchrotron X-ray diffraction. The Ni-O distances are determined from optimization by the density functional theory and used in the calculations. **b**, Sketch of the NiO_6 octahedra. The d_1, d_2, d_3, and d_4 label the corresponding Ni-O distances.

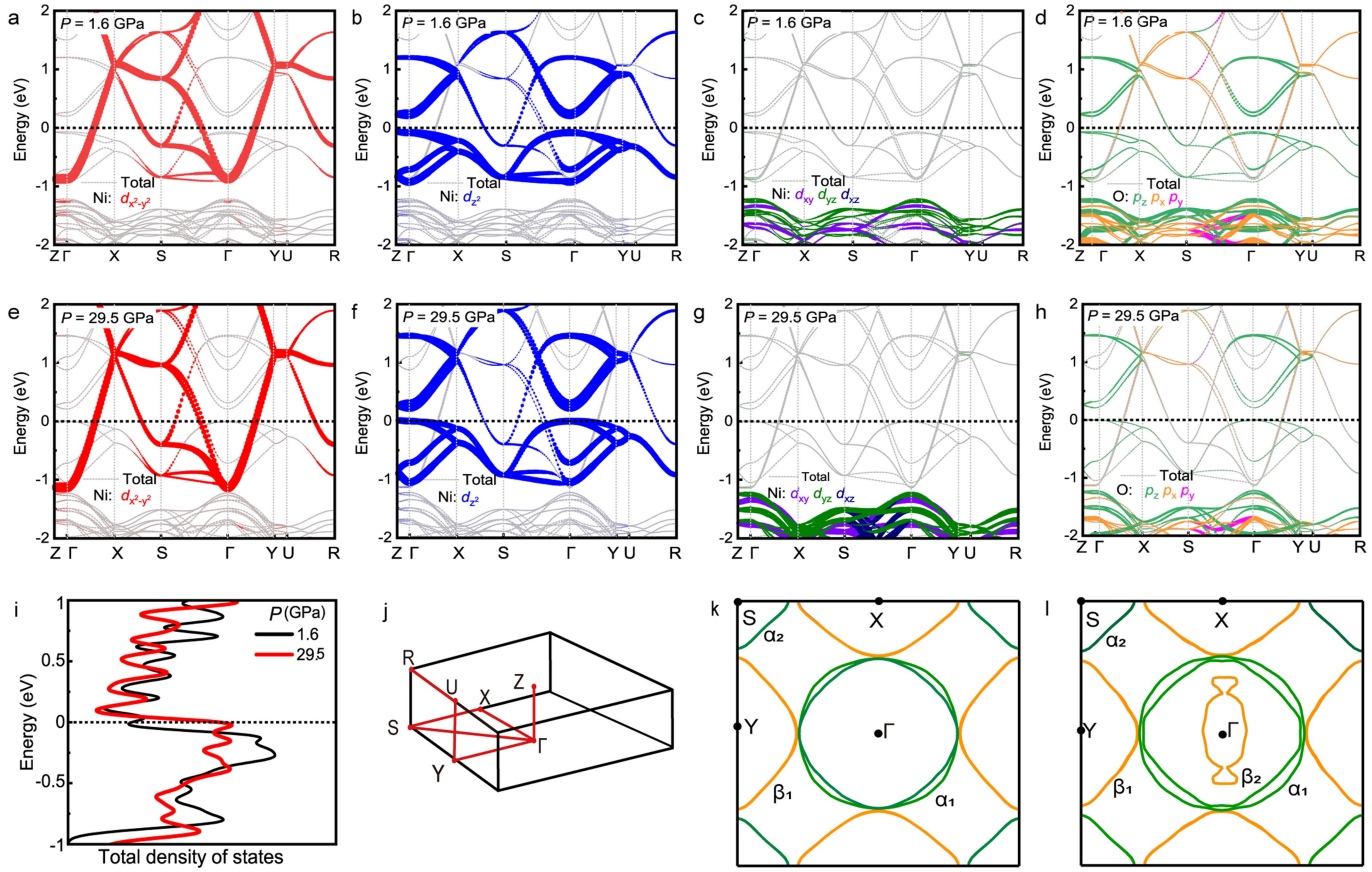

Extended Data Fig. 2 | Density functional theory calculations for $La_3Ni_2O_7$ at 1.6 and 29.5 GPa. a–f, Orbital-decomposed band structures of $La_3Ni_2O_7$ at **a–d** 1.6 GPa and **e–f** 29.5GPa. **i**, The total density of states at 1.6 and 29.5 GPa near the Fermi level. **j**, Schematic of the three-dimensional reciprocal unit cell. The red lines correspond to the paths of the electronic bands. **k**, Calculated two-dimensional Fermi surfaces of $La_3Ni_2O_7$ in a Brillouin zone at 1.6 GPa marked by a black square. The Fermi surfaces consist of electrons bands ($\alpha_{1,2}$) and a hole band (β_1). **l**, Two-dimensional Fermi surfaces of $La_3Ni_2O_7$ at 29.5 GPa. Additional hole bands (Ni $3d_{z^2}$) cross the Fermi level.

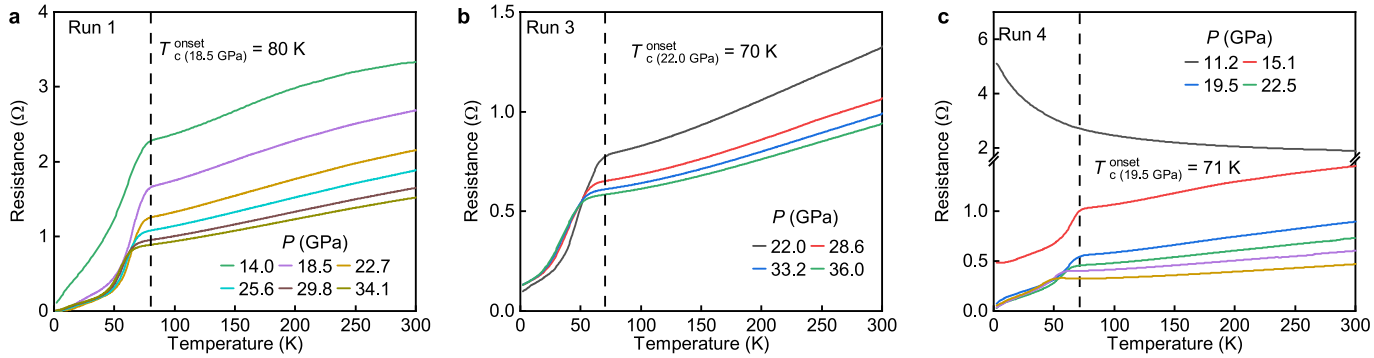

Extended Data Fig. 3 | Resistance measurements of $La_3Ni_2O_7$ single crystals under pressure acquired in different runs. a–**c**, Resistance curves obtained from: **a**, Run 1, **b**, Run 3, and **c**, Run 4 measured with a gasket of cubic boron nitride without a pressure-transmitting medium. The vertical dashed lines indicate the onset superconducting transition temperature T_c. The inset in **a** is a photo showing the electrodes for the high-pressure measurements. A current of 10 μA was used for the measurements.

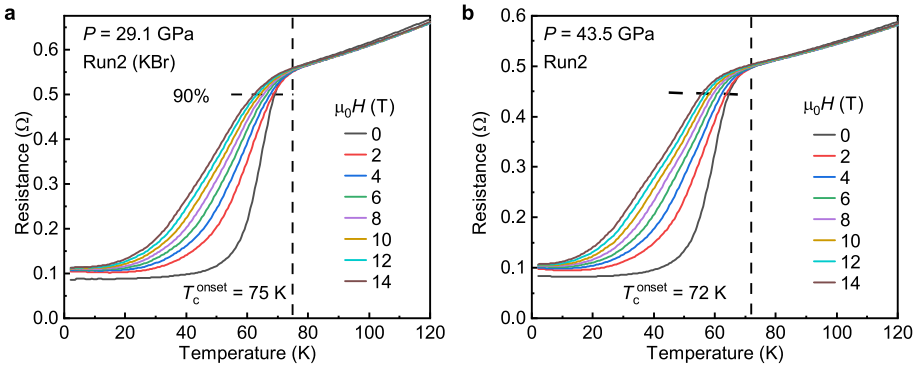

Extended Data Fig. 4 | Suppression of superconductivity of $La_3Ni_2O_7$ by external magnetic fields. a,**b**, Resistance measured at **a**, 29.1 GPa and **b**, 43.5 GPa in the Run 2 with KBr as the pressure transmitting medium. The horizontal dashed lines mark $0.9 \times R(T_c^{onset})$, where $R(T_c^{onset})$ is the resistance at the onset T_c.

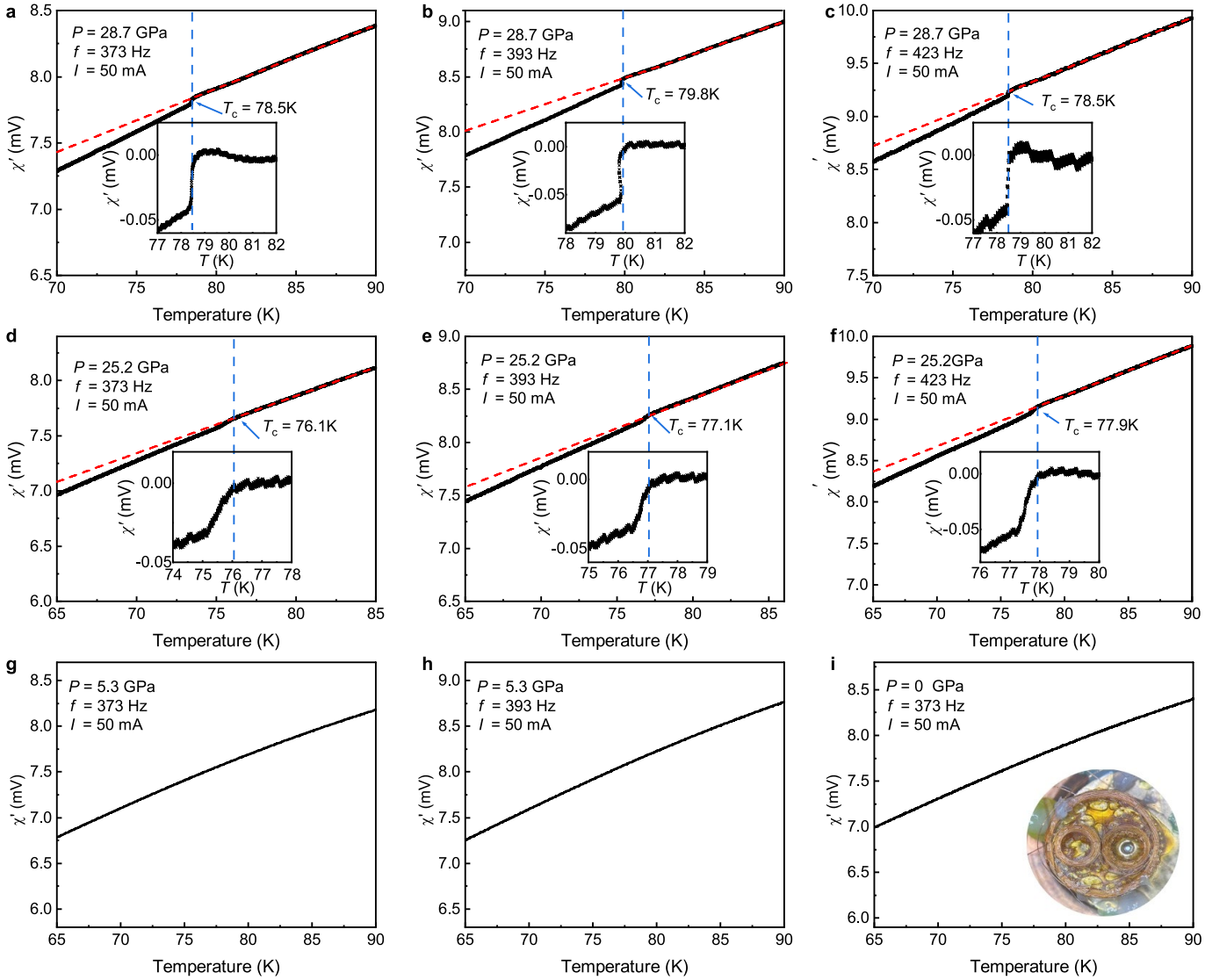

Extended Data Fig. 5 | Diamagnetic response measurements of $La_3Ni_2O_7$ under pressure using the magnetic inductive technique. a–**c**, Raw data of the real part of the *ac* susceptibility showing a prominent diamagnetic response at 28.7 GPa with a current magnitude of 50 mA and frequency of **a** 373, **b** 393, **c** 423 Hz. **d**–**f**, Identical measurements at 25.2 GPa. The red dashed lines are fitted backgrounds following the trend above the superconducting transitions. Insets in **a**–**f** show the diamagnetic signals obtained by subtracting the fitted linear backgrounds. The transition temperature shifts because the pressure changes for each measurement. **g**, **h**, Diamagnetic response measurements at 5.3 GPa measured during the decompressing process with a 373 and 393 Hz frequency current, respectively. **i**, The background measurement of the diamagnetic response of the cell without a sample. The inset in **i** is an image of the experimental set-up for the *ac* susceptibility measurements in a diamond-anvil cell, with a signal coil around the diamond anvils and a neighbor compensating coil.

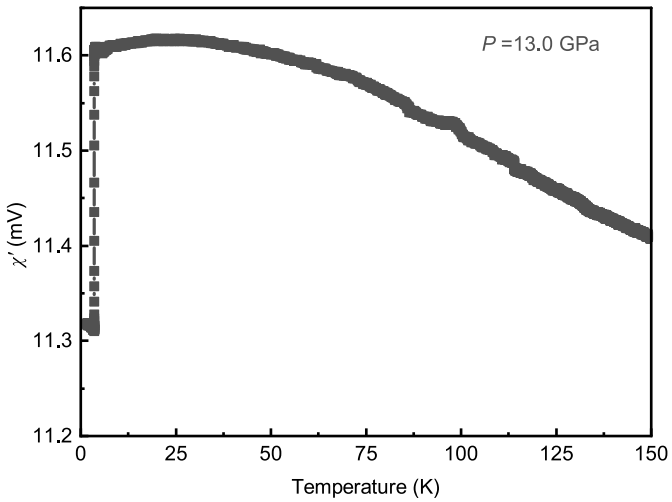

Extended Data Fig. 6 | Magnetic susceptibility of $La_3Ni_2O_7$ measured at 13.0 GPa with the palm-type cubit anvil cell. The sharp drop at 3.6 K corresponds to the superconducting transition of Pb, which is used to calibrate the pressure. No other obvious transitions are reflected from the magnetic susceptibility.

Extended Data Table 1 | Lattice parameters refined from experiments and optimized theoretically

The LP phase at 1.6 GPa, space group: *Amam*				
a = 5.4392 (8), b = 5.3768 (8), and c = 20.403 (4) Å, $\alpha = \beta = \gamma$ =90°, R_{wp} = 9.0%, R_p = 15.7%				
atom	x	y	z	Occ.
Ni	-0.750	0.750 [0.748]	0.401(1) [0.405]	1
La1	-0.250	0.750 [0.758]	0.318 (5) [0.321]	1
La2	-0.750	0.250 [0.248]	0.500	1
O1	-1.000	1.000	0.410	1
O2	-0.750	0.710 [0.719]	0.500	1
O3	-0.500	0.500	0.400 [0.398]	1
O4	-0.750	0.780 [0.781]	0.300 [0.295]	1
The HP- phase at 29.5 GPa, space group: *Fmmm*				
a =5.289 (2) b = 5.218 (2) and c = 19.734 (5) Å, $\alpha = \beta = \gamma$= 90°, R_{wp} = 12.8%, R_p = 16.7%				
atom	x	y	z	Occ.
Ni	0	0	0.089 (2) [0.096]	1
La1	0	0	0.316 (5) [0.321]	1
La2	0	0	0.50	1
O1	0.250	0.250	0.096 [0.095]	1
O2	0	0	0.190 [0.204]	1
O3	0	0	0	1

Refined lattice parameters, atomic coordinates of $La_3Ni_2O_7$ at 1.6 and 29.5 GPa. The values in the brackets are parameters optimized by the density functional theory method and adopted in the calculations.